View Article Online
View Journal

Chemical Science

Accepted Manuscript

This article can be cited before page numbers have been issued, to do this please use: H. Suzuki, A. Nakamura, M. Ikeda, T. Abe, Y. Iida, O. Tomita, M. Higashi, S. Nozawa, A. Saeki and R. Abe, *Chem. Sci.*, 2026, DOI: 10.1039/D6SC02302A.

ROYAL SOCIETY
OF CHEMISTRY

rsc.li/chemical-science

View Article Online
DOI: 10.1039/D6SC02302A

Continually band-tunable bismuth oxyhalides $BiOBr_{1-x}I_x$ as O_2-evolving photocatalysts for visible-light-driven Z-scheme water splitting

Received 00th January 20xx,
Accepted 00th January 20xx

DOI: 10.1039/x0xx00000x

Hajime Suzuki,[a,b,*] Akitoshi Nakamura,[a] Miyuki Ikeda,[a] Toshiki Abe,[a] Yuuki Iida,[a] Osamu Tomita,[a] Masanobu Higashi,[a] Shunsuke Nozawa,[c] Akinori Saeki,[d] and Ryu Abe [a,*]

Continuous and compositionally controllable band-structure tuning remains a central challenge in visible-light-driven photocatalytic water splitting. Here, we demonstrate that layered bismuth oxyhalide solid solutions ($BiOBr_{1-x}I_x$) can provide a continuously tunable platform for rational band engineering in visible-light-driven Z-scheme water splitting. By exploiting the intrinsic halide-dependent band tunability of $BiOBr_{1-x}I_x$ solid solutions, we achieved a balance between extended visible-light absorption and a sufficient reaction thermodynamic driving force. The optimal composition ($x = 0.1$) exhibited sustained O_2 evolution in the presence of Fe^{3+} as a reversible electron acceptor, reflecting the interplay between enhanced visible-light absorption and competing thermodynamic and charge-transport limitations. Suppression of iodine depletion via arc plasma deposition of metallic Pt cocatalysts further enhanced the activity by preserving the composition. When integrated as the O_2-evolving photocatalyst in a Z-scheme system, stoichiometric and steady overall water splitting was achieved for over 50 h under visible light. These findings establish compositionally tunable bismuth oxyhalide solid solutions as versatile materials for rational valence-band engineering in visible-light-driven water splitting.

Introduction

Photocatalytic water splitting with semiconductor materials provides a pathway for sustainable hydrogen production through solar energy conversion.[1-6] Achieving efficient overall water splitting requires precise band-structure engineering to enable visible-light absorption while maintaining appropriate redox energetics. Although various metal oxides have been developed as photocatalysts for ultraviolet-light-driven water splitting,[7-10] tailoring their band energies for efficient visible-light-driven water splitting remains intrinsically challenging. This limitation arises primarily from the dominant contribution of O 2p orbitals to the valence band, which restricts flexible control over band-edge positions.[11] Consequently, significant efforts have focused on incorporating anion orbitals other than O 2p—such as N 2p or S 3p states—into the valence band to raise its maximum to less positive potentials and extend visible-light absorption.[12] Metal oxynitrides, including TaON and $BaTaO_2N$, have demonstrated activity as H_2-evolving photocatalysts in two-step (Z-scheme) water splitting systems or as photoanodes for water oxidation.[13-15] However, continuous and predictable band tuning via O^{2-}/N^{3-} substitution is limited by the difficulty of arbitrary composition control arising from their different valences. Similarly, in oxysulfides, continuous band tuning through O^{2-}/S^{2-} substitution in oxysulfides is often restricted by the substantial mismatch in radii between the two anions. Consequently, the development of photocatalysts that enable continuous anion substitution for band structure tuning while preserving the crystal structure remains a fundamental challenge.

Bismuth oxyhalides, BiOX (X=Cl, Br, I), consisting of positively charged $[Bi_2O_2]^{2+}$ and halogen anions (X^-), have recently attracted attention as band-tunable semiconductors (Figure 1).[16-20] Halogen p orbitals significantly contribute to valence-band formation, and their band structure can be systematically tuned by halide substitution. In particular, BiOBr–BiOI solid solutions ($BiOBr_{1-x}I_x$) allow continuous modulation of the band gap across the visible region through Br^-/I^- substitution. Although such band-tunable solid solutions have been extensively studied for organic pollutant degradation,[18-19] their application in visible-light-driven water splitting, particularly in Z-scheme systems, has not been explored. Herein, we demonstrate the first application of compositionally tunable $BiOBr_{1-x}I_x$ solid solutions as O_2-evolving photocatalysts in visible-light-driven Z-scheme water splitting and provide a strategy for exploiting band-tunable solid solutions in solar-driven water splitting.

---

[a] Department of Energy and Hydrocarbon Chemistry, Graduate School of Engineering, Kyoto University, Katsura, Nishikyo-ku, Kyoto 615-8510, Japan
[b] Precursory Research for Embryonic Science and Technology (PRESTO), Japan Science and Technology Agency (JST), 4-1-8 Honcho, Kawaguchi, Saitama 332-0012, Japan
[c] Photon Factory (PF), Institute of Materials Structure Science (IMSS), High Energy Accelerator Research Organization (KEK), Tsukuba, Ibaraki 305-0801, Japan
[d] Department of Applied Chemistry, Graduate School of Engineering, The University of Osaka, 2-1 Yamadaoka, Suita, Osaka 565-0871, Japan

View Article Online
DOI: 10.1039/D6SC02302A

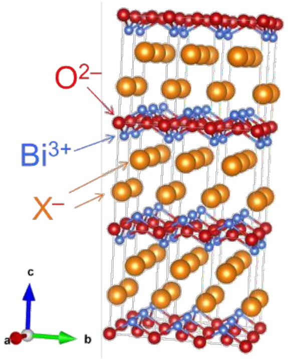

Figure 1. Crystal structure of layered bismuth oxyhalides BiOX (X=Cl, Br, I).

Results and Discussion

Characterization of $BiOBr_{1-x}I_x$ samples

$BiOBr_{1-x}I_x$ (x = 0–1) samples were prepared *via* soft chemical reaction.[21] Figure 2 shows the X-ray diffraction (XRD) patterns of the obtained $BiOBr_{1-x}I_x$ (x = 0–1) samples. No appreciable peaks corresponding to impurity phases were observed in any of the samples. With increasing x values in the $BiOBr_{1-x}I_x$ samples, the diffraction peaks (for example, the (001) diffraction as seen in the enlarged view) gradually shifted toward lower angles, indicating the increase in the lattice constant by introducing I^- anions having a larger ionic radius (ca. 2.20 A) than Br^- (ca. 1.96 A).[22] As shown in Figure S1, the lattice parameter determined by Le Bail refinement of the XRD patterns increased almost linearly with increasing x values, following Vegard's law. The elemental ratios determined by energy-dispersive X-ray spectroscopy (EDX) analysis (I/(Br + I) and I/Bi) were also in good agreement with the nominal compositions (Table S1). In addition, photoelectron yield spectroscopy (PYS) measurements were performed to evaluate the valence-band positions of the $BiOBr_{1-x}I_x$ samples (Figure S2). The ionization potential gradually decreased with increasing iodine content, indicating an upward shift in the valence-band maximum. These results indicate the successful formation of solid solutions of BiOBr and BiOI. As shown in the SEM images (Figure S3), the particle sizes of the $BiOBr_{1-x}I_x$ samples were slightly smaller than those of pure BiOBr.

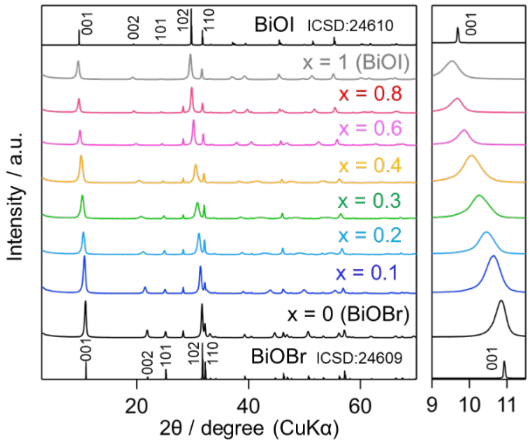

Figure 2. XRD patterns of $BiOBr_{1-x}I_x$ samples (x = 0–1). The inset highlights the systematic shift of the (001) reflection with increasing iodine content.

Figure 3 shows the diffuse reflectance spectra of the $BiOBr_{1-x}I_x$ samples. The absorption edges of the $BiOBr_{1-x}I_x$ samples shift toward longer wavelengths with increasing x, which is attributed to bandgap narrowing induced mainly by an upward shift of the valence band maximum due to the contribution of I 5p orbitals to valence-band formation in conjunction with Br 4p and O 2p orbitals.

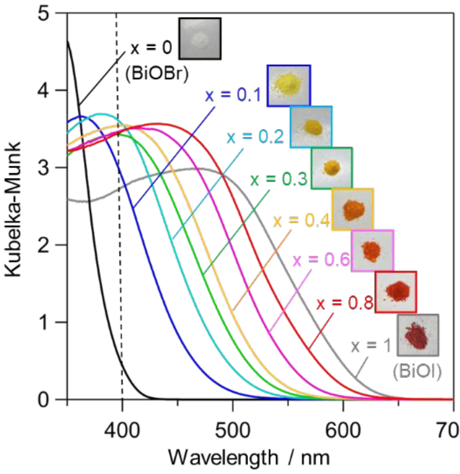

Figure 3. Diffuse reflectance spectra of $BiOBr_{1-x}I_x$ samples, showing progressive red-shift of the absorption edge with increasing iodine content.

Photocatalytic O_2 evolution on UV-responsive BiOBr

The photocatalytic O_2 evolution activity of BiOBr which possesses the largest bandgap (3.0 eV) among the $BiOBr_{1-x}I_x$ species was first evaluated using Fe^{3+} as a reversible electron acceptor under light irradiation ($\lambda > 300$ nm). Herein, Pt species were loaded as a cocatalyst to promote the reduction of Fe^{3+}, followed by a previous study on an oxyhalide O_2 evolution photocatalyst.[23-24] The X-ray absorption fine structure (XAFS) analysis (Figure S4) revealed that the loaded Pt species existed in an intermediate chemical state between metallic Pt and PtO_2. No discernible change in the XRD patterns was observed after Pt loading, confirming that the crystal structure remained intact after cocatalyst deposition (Figure S5). For simplicity, the sample loaded with the Pt species is hereafter referred to as Pt-$BiOBr_{1-x}I_x$. Figure 4 shows the time courses of O_2 evolution from water over the Pt-BiOBr sample using various iron salts ($Fe(NO_3)_3$, $Fe(ClO_4)_3$, $FeCl_3$, and $Fe_2(SO_4)_3$) as sources of Fe^{3+} under UV–visible light irradiation ($\lambda > 300$ nm). For comparison, the activity of unmodified BiOBr without Pt is shown in Figure S6.

View Article Online
DOI: 10.1039/D6SC02302A

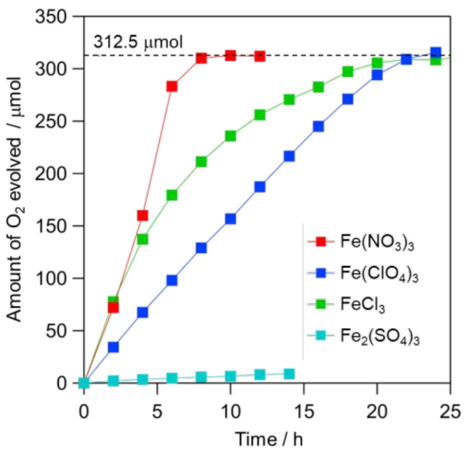

Figure 4. Time courses of photocatalytic O_2 evolution over Pt-BiOBr from aqueous Fe^{3+} solutions (5 mM, 250 mL) with various counter anions under UV–visible light irradiation (λ > 300 nm).

O_2 evolution from aqueous $Fe(NO_3)_3$ and $Fe(ClO_4)_3$ proceeded at almost steady rates until the total amount of O_2 reached ca. 312 µmol. In the present system, the following reactions occur under irradiation:

$BiOBr + h\nu \rightarrow e^- + h^+$ ($h\nu >$ 3.0 eV) (1)

$Fe^{3+} + e^- \rightarrow Fe^{2+}$ (E^0 = +0.77 V vs. SHE) (2)

$2H_2O + 4h^+ \rightarrow O_2 + 4H^+$ (E^0 = +1.23 V vs. SHE) (3)

The saturated amounts of O_2 evolved (*ca.* 312 µmol) agreed well with the stoichiometric value (312.5 µmol) (combination of Eq. 2 and 3) expected from the amount of Fe^{3+} (1250 µmol) added to the solution before irradiation, indicating negligible contributions from side reactions. Figure S7 shows the apparent quantum efficiency of O_2 evolution from an aqueous $Fe(NO_3)_3$ solution under irradiation with monochromatic light. The quantum efficiency increased upon irradiation by monochromatic light with wavelengths shorter than *ca.* 400 nm, in agreement with the absorption spectrum of BiOBr, indicating that O_2 evolution occurred photocatalytically through the bandgap excitation of BiOBr. As shown in Figure 5, no significant change was observed in the XRD patterns of the BiOBr samples after the reaction in aqueous $Fe(NO_3)_3$ and $Fe(ClO_4)_3$. These findings indicate that BiOBr can function as a stable and efficient O_2-evolving photocatalyst in the presence of Fe^{3+}, at least when coupled with appropriate anions, such as NO_3^- or ClO_4^-.

Importantly, steady rates of O_2 evolution from aqueous Fe^{3+} solution with these anions indicates that the oxidation of water, which is thermodynamically less favorable than the oxidation of Fe^{2+} (Eq. 4), proceeded preferentially.

$Fe^{2+} + h^+ \rightarrow Fe^{3+}$ (4)

Figure S8 shows the amounts of Fe^{3+} and Fe^{2+} cations adsorbed on the surfaces of the BiOBr particles in aqueous solutions containing different concentrations of $Fe(ClO_4)_3$ and $Fe(ClO_4)_2$, respectively. Clearly, the amount of Fe^{3+} cations adsorbed on BiOBr was much higher than that of Fe^{2+} at each concentration, strongly suggesting the preferential adsorption of Fe^{3+} on the surface of the BiOBr particles during the reaction, in which both Fe^{3+} and Fe^{2+} cations coexisted. Such preferential adsorption of the electron acceptor Fe^{3+} is undoubtedly beneficial for the preferential oxidation of water to O_2 in the presence of a redox couple in Z-scheme water-splitting systems, as shown in various redox systems.[25-28]

In contrast, the use of Cl^- or SO_4^{2-} anions with Fe^{3+} was detrimental to the stability of the BiOBr photocatalyst. As shown in Figure 4, the rate of O_2 evolution in aqueous $FeCl_3$ gradually decreased during the reaction; the O_2 evolution saturates at a slightly smaller amount (*ca.* 305 µmol) than the expected value. The O_2 evolution on a bare BiOBr sample readily terminates at a much lower amount (*ca.* 100 µmol), as seen in Figure S6. The XRD pattern of BiOBr changed significantly after reaction in aqueous $FeCl_3$ (Figure 5). The intensity of the (001) diffraction peak drastically decreased, whereas peaks corresponding to BiOCl appeared (indicated by asterisks). This change was not observed when the BiOBr particles were stirred in aqueous $FeCl_3$ under dark conditions, indicating that anion exchange from Br^- to Cl^- occurred in connection with the photocatalytic process. Because BiOCl possesses a wider bandgap (3.5 eV) than BiOBr does (3.0 eV),[29] the activity of BiOBr during the reaction in aqueous $FeCl_3$ is lower because of the decreased number of photons that can be absorbed by the photocatalyst particles as a consequence of anion exchange.

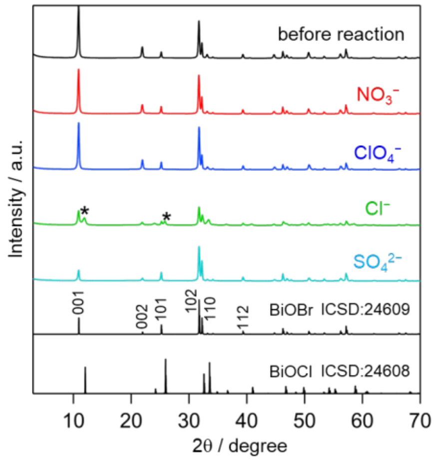

Figure 5. XRD patterns of Pt-BiOBr before and after O_2 evolution from aqueous Fe^{3+} solutions with various counter anions. The asterisks indicate typical peaks derived from BiOCl.

Aqueous $Fe_2(SO_4)_3$ significantly lowered the rate of O_2 evolution, as shown in Figure 4, along with a remarkable decrease in the peak intensity of the (001) diffraction (see Figure 5), suggesting the exfoliation of the bismuth oxide layers by the intercalation of SO_4^{2-} (or HSO_4^-) anions during the reaction. The relatively low rate of O_2 evolution in the initial period suggests that the presence of SO_4^{2-} (or HSO_4^-) itself inhibits O_2 evolution on the BiOBr photocatalyst. Such detrimental effects of SO_4^{2-} anions on O_2 evolution can be explained by the increased overpotential for Fe^{3+} reduction due to the formation of a complex of Fe^{3+} and SO_4^{2-},[30] as has also been discussed for other photocatalysts.[24, 31] For comparison, the O_2 evolution activity of the Pt-free BiOBr sample is shown in Figure S6. Although O_2 evolution was observed without Pt, the activity was consistently enhanced upon Pt loading, whereas the relative trends among the different iron salts remained unchanged.

Photocatalytic O_2 evolution on visible responsive $BiOBr_{1-x}I_x$ solid solutions

Based on the above findings for UV-responsive BiOBr, we extended our investigation to band-tunable $BiOBr_{1-x}I_x$ solid solutions to evaluate their photocatalytic performance under visible-light irradiation. Pt species were also loaded onto each $BiOBr_{1-x}I_x$ solid-solution sample using the impregnation method. XAFS measurements of a representative sample ($BiOBr_{0.9}I_{0.1}$) revealed that the loaded Pt species were in a chemical state intermediate between metallic Pt and PtO_2, similar to the case of BiOBr, and relatively close to that of metallic Pt (Figure 9 and Figure S18). However, in the iodine-containing solid solution, the iodine species were partially removed during the calcination process involved in the impregnation method (Figure 8). Strategies to prevent iodine loss are discussed in the following section. Hereafter, the photocatalytic activities discussed in this section were evaluated using samples prepared by the conventional impregnation method.

Using the optimized reaction conditions established for BiOBr, photocatalytic O_2 evolution was performed in an aqueous $Fe(NO_3)_3$ solution under visible-light irradiation (λ > 400 nm) (Figure 6). Unless otherwise noted, the Pt loading amount was fixed at 0.5 wt%, which was found to be optimal for photocatalytic O_2 evolution (Figure S9). Control experiments using Co- and Mn-based cocatalysts, which are generally known to promote water oxidation, resulted in substantially lower activities (Figure S10), suggesting that efficient Fe^{3+} reduction is essential in the present system. Under UV–visible irradiation (λ > 300 nm) (Figure S11), all solid-solution samples exhibited lower O_2 evolution activity than BiOBr did, and the activity decreased with increasing iodine content. No O_2 evolution was observed for BiOI. In contrast, under visible-light irradiation (λ > 400 nm) (Figure 6), only a negligible amount of O_2 evolved over BiOBr, which absorbed hardly any visible light. The introduction of a small amount of iodine markedly enhanced the O_2 evolution. These results clearly demonstrate that the solid-solution strategy enables effective utilization of visible light for photocatalytic O_2 evolution. Among the solid solutions, the activity reached a maximum at x = 0.1 and decreased with a further increase in iodine content. Additional activity comparisons using x = 0.05 and 0.15 (Figure S12) confirmed that $BiOBr_{0.9}I_{0.1}$ exhibited the highest photocatalytic performance. Thus, the activity increased with bandgap narrowing up to x = 0.1 due to the extended visible-light absorption, whereas further iodine incorporation led to activity deterioration.

View Article Online
DOI: 10.1039/D6SC02302A

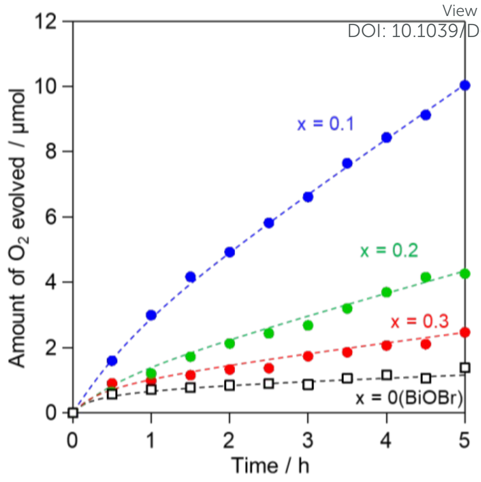

Figure 6. Time courses of photocatalytic O_2 evolution over Pt-$BiOBr_{1-x}I_x$ from aqueous $Fe(NO_3)_3$ solution (1 mM, 250 mL) under visible light (λ > 400 nm).

Two possible factors can account for this decline: (1) reduced thermodynamic driving force due to band-level shifts and (2) decreased crystallinity caused by iodine substitution. Regarding the first factor, previous reports have indicated that iodine incorporation shifts the valence-band maximum to more negative potentials and the conduction-band minimum to more positive potentials (Figure S13).[29] Consequently, increasing iodine content reduces the driving force for both Fe^{3+} reduction and water oxidation. Based on the reported band structures and measured ionization potentials (Figure S2), the shift in the valence-band maximum contributed to a reduced driving force for water oxidation, which likely played a key role in the observed activity decline. Regarding the second factor, the XRD patterns (Figure 2) show progressive peak broadening with increasing iodine content from x = 0 to 0.3. The crystallite size estimated from the full width at half-maximum of the (001) diffraction peak using the Scherrer equation decreased significantly from 251 Å (x = 0) to 148 Å (x = 0.3) (Table S2). The deterioration of crystallinity was further evidenced by time-resolved microwave conductivity (TRMC) measurements.[32-35] The TRMC signal corresponds to the product of the charge carrier generation yield (φ) and the sum of carrier mobilities ($\Sigma\mu$). Because these materials are n-type semiconductors, and the effective mass of electrons is smaller than that of holes, the TRMC response predominantly reflects the electron transport properties. As shown in Figure 7a, the photoconductivity signal markedly decreased with increasing iodine content, which is consistent with the reduction in crystallite size. The maximum $\varphi\Sigma\mu$ values (Figure 7b) indicate that iodine substitution lowers carrier generation efficiency and/or mobility. Therefore, the enhanced charge trapping and recombination associated with the decreased crystallinity likely constitutes another key factor responsible for the reduced activity at higher iodine contents.

View Article Online
DOI: 10.1039/D6SC02302A

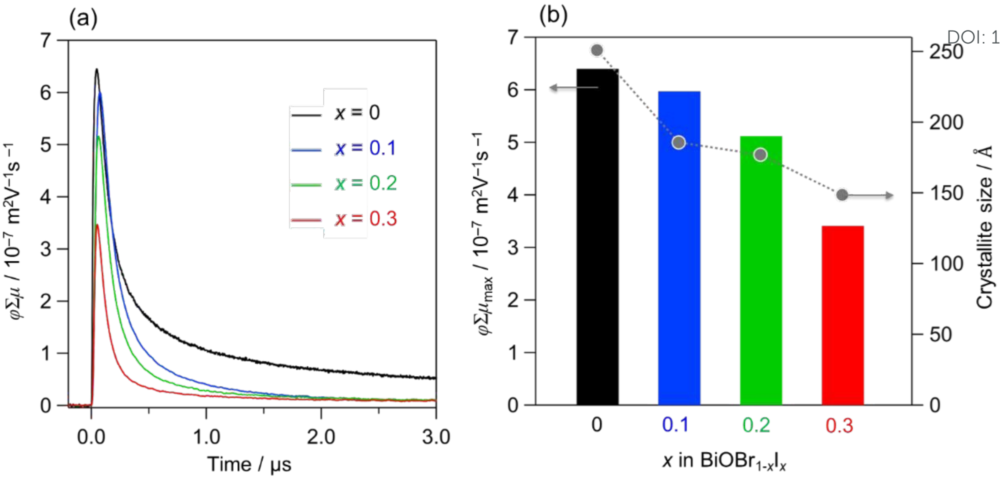

Figure 7. (a) TRMC kinetics of $BiOBr_{1-x}I_x$ samples (x = 0, 0.1, 0.2, 0.3) (λ_{ex} = 355 nm, $I_0 = 4.6 \times 10^{15}$ photons cm^{-2} $pulse^{-1}$). (b) TRMC signal maximum ($\varphi\Sigma\mu_{max}$) and crystallite size calculated from the full width at half-maximum of the (001) diffraction peak.

Using Pt-loaded $BiOBr_{0.9}I_{0.1}$, prolonged photocatalytic O_2 evolution was performed in a 1 mM $Fe(NO_3)_3$ aqueous solution (Figure S14). After 40 h of reaction, 32 µmol of O_2 was evolved. Because water oxidation is a four-electron process, this corresponds to 128 µmol of electrons transferred during the reaction. The amount of photocatalyst used was 50 mg, which contains 16.2 µmol of iodide ions. The total number of electrons transferred during the reaction significantly exceeded the total iodide content of the photocatalyst. Furthermore, XRD analysis after the long-term reaction confirmed that the crystal structure was retained with no detectable peak shift (Figure S15). These results demonstrate that the solid solution state was preserved and that $BiOBr_{0.9}I_{0.1}$ exhibited sustained O_2 evolution over an extended period.

Arc plasma deposition of Pt Cocatalyst on $BiOBr_{0.9}I_{0.1}$

In the previous section, Pt species were loaded onto $BiOBr_{0.9}I_{0.1}$ by the conventional impregnation method. However, significant iodine loss occurred during the calcination process. As shown in Figure 8a, the XRD peaks shifted toward higher angles after impregnation loading, indicating compositional changes. XPS analysis of the I $3d_{5/2}$ region further revealed a substantial decrease in the iodine content (Figure 8b). Therefore, for iodine-containing solid solutions, a Pt-loading method that avoids calcination is required to preserve iodine and improve photocatalytic performance.

We recently reported an arc plasma deposition method that enables the loading of metallic Pt nanoparticles without heat treatment.[36] In this method, nanosized Pt particles are uniformly deposited via arc discharge and the chemical state of Pt can be controlled by adjusting the gas atmosphere. For example, deposition under H_2 flow enables the reductive loading of metallic Pt. Pt-loaded TiO_2 prepared by this method exhibited higher H_2 evolution activity than samples prepared by conventional methods.[36] Accordingly, metallic Pt nanoparticles were loaded onto $BiOBr_{0.9}I_{0.1}$ by arc plasma deposition under a H_2 flow. As shown in Figure 9a (see also Figures S16 and S17 for additional regions), Pt nanoparticles smaller than 10 nm were uniformly dispersed on the photocatalyst surface. Similar particle sizes were observed in the impregnation-loaded samples. XANES analysis (Figure 9b) confirmed that the Pt species deposited by arc plasma were predominantly in the metallic state, similar to those in the impregnation-loaded samples. This finding is further supported by the EXAFS results (Figure S18). Importantly, XPS analysis of the I $3d_{5/2}$ region (Figure 8b) showed that the peak intensity of Pt-$BiOBr_{0.9}I_{0.1}$ prepared by arc plasma deposition was almost identical to that of pristine $BiOBr_{0.9}I_{0.1}$, indicating that iodine was preserved during the loading process. Thus, arc plasma deposition successfully deposited metallic Pt nanoparticles onto $BiOBr_{0.9}I_{0.1}$ without inducing iodine loss.

Photocatalytic O_2 evolution in the $Fe(NO_3)_3$ solution is shown in Figure S19, and the O_2 amount after 5 h is summarized in Figure 9c. The arc plasma-loaded sample exhibited a 2.5-fold higher O_2 evolution rate than the impregnation-loaded sample. This enhancement is attributed to the suppression of iodine loss due to the absence of calcination treatment. The retention of iodine during the photocatalytic reaction was also confirmed by EDX analysis (Table S3). The XRD patterns after the reaction showed no significant change or peak shift (Figure S20), further supporting the structural stability and retention of iodine during photocatalysis. In addition, the generation of Fe^{2+} species corresponding to the evolved O_2 was confirmed by absorption spectroscopy (Figure S21), supporting electron transfer from the photocatalyst to Fe^{3+} ions. The apparent quantum efficiency (AQE) for O_2 evolution under monochromatic irradiation at 405 nm was 0.7%. Although this value is still lower than those reported for some reported Sillén-type oxyhalide photocatalysts (Table S4), further improvements may be achieved through optimization of the cocatalyst and reaction system.

View Article Online
DOI: 10.1039/D6SC02302A

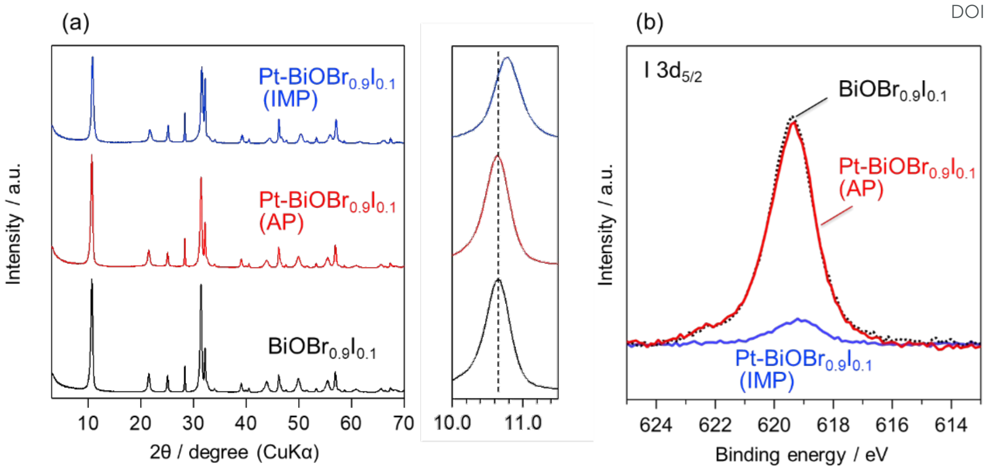

Figure 8. (a) XRD pattern and (b) I 3d$_{5/2}$ XPS profile of BiOBr$_{0.9}$I$_{0.1}$ before and after Pt loading via arc plasma (AP) and impregnation (IMP) methods.

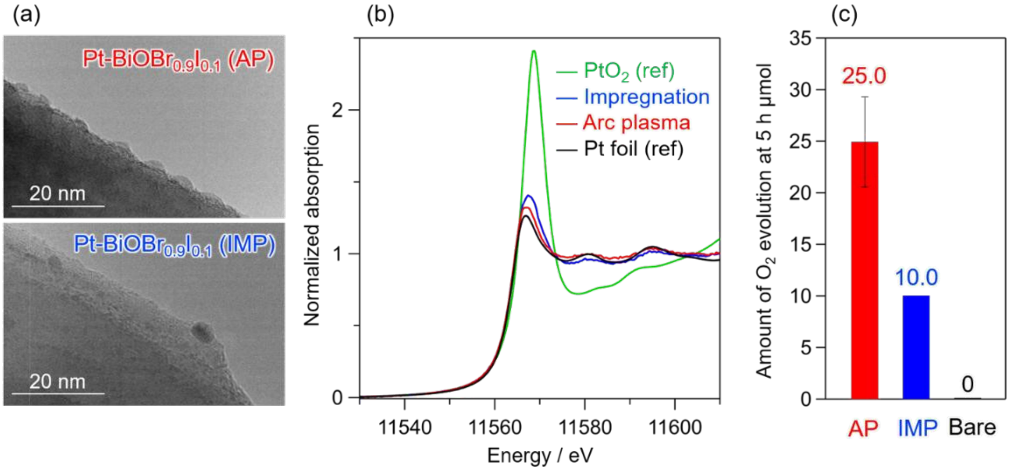

Figure 9. (a) TEM image of Pt-BiOBr$_{0.9}$I$_{0.1}$ prepared by arc plasma (AP) and impregnation (IMP) methods. (b) Pt L3-edge XANES spectra of the samples, along with those of Pt foil and PtO$_2$. (c) Photocatalytic O$_2$ evolution amounts over the samples from aqueous Fe(NO$_3$)$_3$ solution (1 mM) under visible light irradiation (λ > 400 nm). Error bars represent the standard error.

Visible-light-driven Z-scheme water splitting using BiOBr$_{1-x}$I$_x$ as an O$_2$-evolving photocatalyst

To verify the feasibility of Z-scheme water splitting, BiOBr$_{0.9}$I$_{0.1}$ loaded with Pt via arc plasma deposition was employed as an O$_2$-evolving photocatalyst in a visible-light-driven Z-scheme water splitting system. Rh-doped SrTiO$_3$ (SrTiO$_3$:Rh; Figure S22), which exhibits high activity in Fe redox systems, was used as the H$_2$-evolving photocatalyst.[37] Under visible-light irradiation in the presence of the Fe^{3+}/Fe^{2+} redox mediator, the stoichiometric evolution of H$_2$ and O$_2$ with an approximate 2:1 ratio was sustained over 54 h (Figure 10). These results clearly demonstrate that the BiOBr$_{1-x}$I$_x$ solid solution can function as an O$_2$-evolving photocatalyst in a visible-light-driven Z-scheme water-splitting system (Figure S23).

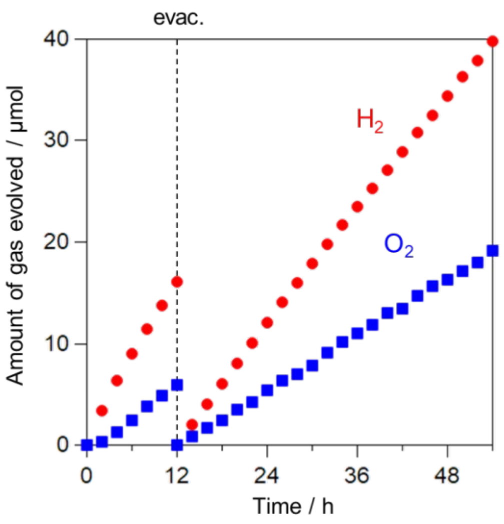

Figure 10. Z-scheme water splitting using a mixture of Ru–SrTiO$_3$:Rh (0.1 g) and Pt-BiOBr$_{0.9}$I$_{0.1}$ (0.1 g) in an aqueous solution with Fe(NO$_3$)$_3$ (2 mM) under visible-light irradiation (λ > 400 nm).

View Article Online
DOI: 10.1039/D6SC02302A

Conclusions

We demonstrated the first application of compositionally tunable $BiOBr_{1-x}I_x$ solid solutions as O_2-evolving photocatalysts for visible-light-driven Z-scheme water splitting. By leveraging the intrinsic halide-dependent band tunability, controlled iodine substitution enabled systematic modulation of the band structure, extending visible-light absorption while maintaining a sufficient thermodynamic reaction driving force. The optimal composition (x = 0.1) reflects a balance between enhanced light harvesting and competing thermodynamic and charge-transport limitations, highlighting the interplay between band engineering and crystallinity in governing the photocatalytic activity. The arc plasma deposition of metallic Pt nanoparticles suppressed iodine loss during cocatalyst loading and significantly enhanced the O_2 evolution activity, underscoring the critical role of compositional integrity in halide-containing photocatalysts. The successful demonstration of stable water splitting under visible light establishes the BiOX solid solutions as O_2-evolving components in a Z-scheme system. More broadly, this study identifies layered bismuth oxyhalide solid solutions with mixed halides as a viable strategy for continuous and structurally compatible band-structure engineering in visible-light-driven water splitting.

Experimental Section

Preparation of photocatalyst samples

Particles of $BiOBr_{1-x}I_x$ (x = 0–1) were synthesized *via* a soft-chemical method according to a previous report.[21] For the preparation of pure BiOBr particles, NaBr (32.8 mmol, 99.9%, Wako Pure Chemical Industries, Ltd.) was first dissolved into distilled water (37.5 mL) with CH_3COONa (65.6 mmol, 98.5%, Wako Pure Chemical Industries, Ltd.). Another solution was prepared in parallel as a bismuth source, in which $Bi(NO_3)_3{\cdot}5H_2O$ (32.8 mmol, 99.9%, Wako Pure Chemical Industries, Ltd.) was dissolved in glacial acetic acid (2.5 mL, 99.5%, Wako Pure Chemical Industries, Ltd.). The two solutions were combined and stirred for 20 h at room temperature. The precipitate was collected via centrifugation, washed twice with pure water, and dried at 393 K in air for 5 h. To prepare particles of the solid solution $BiOBr_{1-x}I_x$ (x = 0–0.8), a mixture of NaBr and NaI (total 32.8 mmol with a molar ratio of 1-x : x) was used as the precursor, dissolved in distilled water with CH_3COONa, and then subjected to the same procedures as for the pure samples shown above.

The platinum species were loaded on BiOBr as a cocatalyst *via* a conventional impregnation method using an aqueous solution of hydrogen hexachloroplatinate (IV) hexahydrate ($H_2PtCl_6{\cdot}6H_2O$, 99.9%, Wako Pure Chemical Industries, Ltd.) as a precursor, followed by calcination in air at 623 K for 1 h. The amount of Pt-based cocatalyst was set to be 0.5 wt% as Pt metal. For $BiOBr_{1-x}I_x$ solid-solution samples, the platinum species were loaded using $Pt(NH_3)_4(OH)_2$ (Furuya Metal Co., Ltd.) as the precursor under the same impregnation and calcination conditions to prevent substitution of I^- by Cl^- originating from the precursor.[38] When comparing the photocatalytic activities of the solid-solution samples and BiOBr, the Pt-based cocatalyst was also loaded onto BiOBr using $Pt(NH_3)_4(OH)_2$ under the same conditions. For $BiOBr_{0.9}I_{0.1}$, the Pt species were also loaded by means of arc plasma deposition.[36] The $BiOBr_{0.9}I_{0.1}$ particles were subjected to the deposition of the Pt species (0.5 wt% as Pt metal) using a pulsed cathodic arc plasma source (ULVAC, APD-SP) with a Pt cathode (99.9%, Kojundo Chemical Laboratory Co., Ltd.) under the following conditions: condenser capacitance, 1800 μF; applied voltage, 100 V; chamber pressure, ~6.0 Pa; H_2 flow rate, 10 sccm.

Particles of $SrTiO_3$ doped with Rh (1 mol% relative to Ti), designated as $SrTiO_3$:Rh, were prepared by a solid-state reaction according to the previous report,[37] using $SrCO_3$ (99.99%, Wako Pure Chemical Industries, Ltd.), TiO_2 (rutile, 99.9%, Wako Pure Chemical Industries, Ltd.), and Rh_2O_3 (≥98.0%, Wako Pure Chemical Industries, Ltd.) as raw materials. These materials were mixed at a Sr:Ti:Rh molar ratio of 1.00:0.99:0.01 and calcined at 1273 K for 10 h. The structural and optical characterizations of the obtained $SrTiO_3$:Rh sample are shown in Figure S22. Deposition of a Ru cocatalyst on $SrTiO_3$:Rh was carried out by means of a photodeposition method using $RuCl_3{\cdot}nH_2O$ (85.0% (anhydrous), Wako Pure Chemical Industries, Ltd.) as a precursor.[39]

Characterization of photocatalyst samples

The obtained particles were characterized by X-ray diffraction (XRD; MiniFlex II, Rigaku Corp., Cu Kα radiation, unless otherwise noted), a UV–visible diffuse reflectance spectroscopy (UV–vis. DRS, V-670, Jasco), a scanning electron microscopy (SEM; VE 9800, KEYENCE), and a transmission electron microscopy (TEM; JEM-2100F, JEOL). The ionization energy was directly measured by photoelectron yield spectroscopy (PYS; BIP-KV201, Bunkoukeiki) in a vacuum ($< 5 \times 10^{-2}$ Pa). The specific surface areas of the samples were measured using N_2 adsorption (BELSORP-mini, BEL Japan) at 77 K. The chemical states of elements were analyzed using X-ray photoelectron spectroscopy (XPS; Model 5500, ULVAC-PHI) with a Mg Kα X-ray source. The binding energies determined by XPS were corrected with reference to the adventitious carbon (C 1s) peak (284.6 eV) for each sample. XAFS measurements were performed at the BL9C beamline of the Photon Factory (High Energy Accelerator Research Organization, Tsukuba, Japan). The X-ray energy was varied using an Si(111) double-crystal monochromator. Reference samples were diluted in boron nitride, compressed to form pellets, and measured in transmission mode. Pt-loaded samples were measured in fluorescence mode using a multichannel solid-state detector. The adsorption amounts of Fe^{3+} and Fe^{2+} were evaluated according to a previously reported procedure.[40] BiOBr powder (15 mg) was dispersed in 15 mL of aqueous $Fe(ClO_4)_3$ (70.0% as $Fe(ClO_4)_3$, Wako Pure Chemical Industries, Ltd.) or $Fe(ClO_4)_2$ (90.0%, Wako Pure Chemical Industries, Ltd.) at a prescribed concentration and stirred in the dark for 3 h in a Pyrex test tube. The concentrations of Fe^{3+} and Fe^{2+} remaining in the supernatant were determined by UV–vis absorption spectroscopy. The crystal structures were visualized using the VESTA program.[41] Le Bail analysis was conducted using JANA2006.[42]

View Article Online
DOI: 10.1039/D6SC02302A

Time-Resolved Microwave Conductivity (TRMC) Measurements

TRMC measurements were carried out in air at room temperature using the third-harmonic generator (355 nm, 4.6 × 10^{15} photons cm^{-2} $pulse^{-1}$) of a Nd:YAG laser (Surelite II, Continuum, 5–8 ns pulse duration, 10 Hz) as the excitation source and X-band microwaves (3 mW, ~9.1 GHz) as the probe. The powdered samples were fixed to quartz substrates using an optically transparent adhesive tape (the tape did not interfere with any TRMC signal). The photoconductivity, $\Delta\sigma$, was calculated using $\Delta\sigma = \Delta P_r/(AP_r)$, where ΔP_r, A, and P_r are the transient power change of the reflected microwave, sensitivity factor, and power of the reflected microwave, respectively. The obtained photoconductivity ($\Delta\sigma$) was converted to the product of the quantum yield (φ) and the sum of the charge-carrier mobilities $\Sigma\mu$ (= $\mu_+ + \mu_-$) by applying the following formula: $\varphi\Sigma\mu = \varphi\Sigma\mu = \Delta\sigma(eI_0F_{light})^{-1}$, where e, I_0, and F_{light} are the unit charge of a single electron, incident photon density of the excitation laser, and correction (or filling) factor, respectively.

Photocatalytic reactions

Photocatalytic O_2 evolution was performed in a Pyrex reaction vessel connected to a closed gas-circulating system. The photocatalyst powder (0.1 g) was suspended in distilled water (250 mL) under magnetic stirring. Iron salts were added in calculated amounts to obtain Fe^{3+} concentrations of 1 or 5 mM. The Fe^{3+} sources employed were $Fe(NO_3)_3\cdot9H_2O$ (99.9%, Wako Pure Chemical Industries, Ltd.), $Fe(ClO_4)_3\cdot nH_2O$ (70.0% as $Fe(ClO_4)_3$, Wako Pure Chemical Industries, Ltd.), $FeCl_3\cdot6H_2O$ (99.0%, Wako Pure Chemical Industries, Ltd.), and $Fe_2(SO_4)_3\cdot nH_2O$ (70% as $Fe_2(SO_4)_3$, Wako Pure Chemical Industries, Ltd.). To prevent the hydrolysis and precipitation of Fe^{3+} species, the pH of the reaction solution was adjusted to approximately 2.4 before irradiation by adding a small amount of the corresponding acid (HNO_3, $HClO_4$, HCl, or H_2SO_4, respectively). For visible-light-driven Z-scheme water splitting employing the Fe^{3+}/Fe^{2+} redox couple, Ru-loaded $SrTiO_3$:Rh (0.1 g) and Pt-loaded $BiOBr_{0.9}I_{0.1}$ prepared by arc plasma deposition (0.1 g) were suspended together in an aqueous $Fe(NO_3)_3$ solution (2 mM, 250 mL) under magnetic stirring. After the solution was thoroughly degassed, Ar gas (5 kPa) was introduced. The suspension was irradiated with a 300 W Xe lamp equipped with a cold mirror, emitting light with wavelengths longer than 300 nm. For visible light irradiation (λ > 400 nm), a cutoff filter (HOYA, L-42) was used. The reaction temperature was maintained at 288 K using circulating water. The evolved gases were analyzed by online gas chromatography (detector: TCD, column packing: molecular sieve 5 A, Ar carrier). The apparent quantum efficiency (AQE) for O_2 evolution of $BiOBr_{0.9}I_{0.1}$ was measured using monochromatic LED light (controller (power): CL-1501; LED heads: CLH1-405-9-1-B (λ = 405 ± 8 nm); head top: CL-H1LCB02, Asahi Spectra Co., Ltd.). The AQE was calculated using the following equation: AQE (%) = $(4 \times R/I) \times 100$, where R and I represent the rate of O_2 evolution and the rate of incident photons measured using a power meter (3664 optical power meter, HIOKI E.E. CORPORATION), respectively.

Conflicts of interest

There are no conflicts to declare.

Data availability

All data are available in the main manuscript and the ESI.

Acknowledgements

This work was supported by JST PRESTO (JPMJPR25M8) and JSPS KAKENHI Grant-in-Aid for Scientific Research (A) (JP20H00398) and (B) (JP23H02061, JP26K01604). This study was also supported by The Samco Foundation. The XAFS experiments were performed with the approval of the Photon Factory Program Advisory Committee (Proposal No. 2024G638). The authors acknowledge Dr. Rie Haruki of the High Energy Accelerator Research Organization (KEK) for assistance with XAFS measurements

References

1 A. Fujishima, K. Honda, *Nature*, 1972, **238**, 37–38.
2 A. Kudo, Y. Miseki, *Chem. Soc. Rev.*, 2009, **38**, 253–278.
3 R. Abe, *J. Photochem. Photobiol. C*, 2010, **11**, 179–209.
4 F. E. Osterloh, *Chem. Soc. Rev.*, 2013, **42**, 2294–2320.
5 S. S. Chen, T. Takata, K. Domen, *Nat. Rev. Mater.*, 2017, **2**, 17050.
6 Y. O. Wang, H. Suzuki, J. J. Xie, O. Tomita, D. J. Martin, M. Higashi, D. Kong, R. Abe, J. W. Tang, *Chem. Rev.*, 2018, **118**, 5201–5241.
7 T. Takata, J. Jiang, Y. Sakata, M. Nakabayashi, N. Shibata, V. Nandal, K. Seki, T. Hisatomi, K. Domen, *Nature*, 2020, **581**, 411–414.
8 H. Kato, K. Asakura, A. Kudo, *J. Am. Chem. Soc.*, 2003, **125**, 3082–3089.
9 Y. Sakata, T. Hayashi, R. Yasunaga, N. Yanaga, H. Imamura, *Chem. Commun.*, 2015, **51**, 12935–12938.
10 Y. Hiramachi, H. Fujimori, A. Yamakata, Y. Sakata, *ChemCatChem*, 2019, **11**, 6213–6217.
11 D. E. Scaife, *Sol. Energy*, 1980, **25**, 41–54.
12 A. Miyoshi, K. Maeda, *Sol. RRL*, 2020, **5**, 2000521.
13 R. Abe, M. Higashi, K. Domen, *ChemSusChem*, 2011, **4**, 228–237.
14 M. Higashi, K. Domen, R. Abe, *J. Am. Chem. Soc.*, 2012, **134**, 6968–6971.
15 M. Higashi, R. Abe, T. Takata, K. Domen, *Chem. Mater.*, 2009, **21**, 1543–1549.
16 X. Zhang, C. Y. Wang, L. W. Wang, G. X. Huang, W. K. Wang, H. Q. Yu, *Sci. Rep.*, 2016, **6**, 22800.
17 X. Cao, A. Huang, C. Liang, H. C. Chen, T. Han, R. Lin, Q. Peng, Z. Zhuang, R. Shen, H. M. Chen, Y. Yu, C. Chen, Y. Li, *J. Am. Chem. Soc.*, 2022, **144**, 3386–3397.
18 X. Zhang, L. W. Wang, C. Y. Wang, W. K. Wang, Y. L. Chen, Y. X. Huang, W. W. Li, Y. J. Feng, H. Q. Yu, *Chem. Eur. J.*, 2015, **21**, 11872–11877.
19 Q. Wang, Z. Liu, D. Liu, G. Liu, M. Yang, F. Cui, W. Wang, *Appl. Catal. B*, 2018, **236**, 222–232.

View Article Online
DOI: 10.1039/D6SC02302A

20 Y. Shi, J. Li, C. Mao, S. Liu, X. Wang, X. Liu, S. Zhao, X. Liu, Y. Huang, L. Zhang, *Nat. Commun.*, 2021, **12**, 5923.
21 K. Ren, J. Liu, J. Liang, K. Zhang, X. Zheng, H. Luo, Y. Huang, P. Liu, X. Yu, *Dalton Trans.*, 2013, **42**, 9706–9712.
22 R. D. Shannon, *Acta Crystallogr., Sect. A*, 1976, **32**, 751–767.
23 K. Ogawa, A. Nakada, H. Suzuki, O. Tomita, M. Higashi, A. Saeki, H. Kageyama, R. Abe, *ACS Appl. Mater. Interfaces*, 2019, **11**, 5642–5650.
24 H. Suzuki, H. Kunioku, M. Higashi, O. Tomita, D. Kato, H. Kageyama, R. Abe, *Chem. Mater.*, 2018, **30**, 5862–5869.
25 R. Abe, K. Sayama, H. Sugihara, *J. Phys. Chem. B*, 2005, **109**, 16052–16061.
26 K. Tsuji, O. Tomita, M. Higashi, R. Abe, *ChemSusChem*, 2016, **9**, 2201–2208.
27 R. Abe, *Bull. Chem. Soc. Jpn.*, 2011, **84**, 1000–1030.
28 K. Ogawa, O. Tomita, K. Takagi, A. Nakada, M. Higashi, R. Abe, *Chem. Lett.*, 2018, **47**, 985–988.
29 Y. Ishii, H. Suzuki, O. Tomita, A. Nakada, R. Abe, *Phys. Chem. Chem. Phys.*, 2026, **28**, 38–41.
30 Y. Miseki, H. Kusama, H. Sugihara, K. Sayama, *Chem. Lett.*, 2010, **39**, 846–847.
31 H. Suzuki, O. Tomita, M. Higashi, R. Abe, *J. Mater. Chem. A*, 2017, **5**, 10280–10288.
32 A. Saeki, M. Tsuji, S. Seki, *Adv. Energy Mater.*, 2011, **1**, 661–669.
33 A. Saeki, S. Yoshikawa, M. Tsuji, Y. Koizumi, M. Ide, C. Vijayakumar, S. Seki, *J. Am. Chem. Soc.*, 2012, **134**, 19035–19042.
34 H. Suzuki, M. Higashi, H. Kunioku, R. Abe, A. Saeki, *ACS Energy Lett.*, 2019, **4**, 1572–1578.
35 H. Suzuki, S. Kanno, M. Hada, R. Abe, A. Saeki, *Chem. Mater.*, 2020, **32**, 4166–4173.
36 H. Suzuki, T. Abe, T. Otsubo, Y. Watanabe, O. Tomita, M. Higashi, A. Saeki, R. Abe, *J. Phys. Chem. C*, 2024, **128**, 4924–4933.
37 R. Konta, T. Ishii, H. Kato, A. Kudo, *J. Phys. Chem. B*, 2004, **108**, 8992–8995.
38 R. Takahashi, M. Ogawa, H. Suzuki, O. Tomita, A. Nakada, S. Nozawa, A. Saeki, R. Abe, *Inorg. Chem.*, 2025, **64**, 9163–9171.
39 Y. Sasaki, A. Iwase, H. Kato, A. Kudo, *J. Catal.*, 2008, **259**, 133–137.
40 T. Ohno, D. Haga, K. Fujihara, K. Kaizaki, M. Matsumura, *J. Phys. Chem. B*, 1997, **101**, 6415–6419.
41 K. Momma, F. Izumi, *J. Appl. Crystallogr.*, 2011, **44**, 1272–1276.
42 V. Petricek, M. Dusek, L. Palatinus, *Z. Kristallogr.*, 2014, **229**, 345–352.

View Article Online
DOI: 10.1039/D6SC02302A

The data supporting this article have been included as part of the Supplementary Information.